Numerical Simulation of Free Surface by an Area-Preserving Level Set Method

Tony W. H. Sheu[1,2,3,*] and C. H. Yu[1]

[1] *Department of Engineering Science and Ocean Engineering, National Taiwan University, No. 1, Sec. 4, Roosevelt Road, Taipei, Taiwan.*
[2] *Taida Institute of Mathematical Sciences (TIMS), National Taiwan University.*
[3] *Center for Quantum Science and Engineering (CQSE), National Taiwan University.*

Abstract. We apply in this study an area preserving level set method to simulate gas/water interface flow. For the sake of accuracy, the spatial derivative terms in the equations of motion for an incompressible fluid flow are approximated by the fifth-order accurate upwinding combined compact difference (UCCD) scheme. This scheme development employs two coupled equations to calculate the first- and second-order derivative terms in the momentum equations. For accurately predicting the level set value, the interface tracking scheme is also developed to minimize phase error of the first-order derivative term shown in the pure advection equation. For the purpose of retaining the long-term accurate Hamiltonian in the advection equation for the level set function, the time derivative term is discretized by the sixth-order accurate symplectic Runge-Kutta scheme. Also, to keep as a distance function for ensuring the front having a finite thickness for all time, the re-initialization equation is used. For the verification of the optimized UCCD scheme for the pure advection equation, two benchmark problems have been chosen to investigate in this study. The level set method with excellent area conservation property proposed for capturing the interface in incompressible fluid flows is also verified by solving the dam-break, Rayleigh-Taylor instability, two-bubble rising in water, and droplet falling problems.

AMS subject classifications: 65E05, 76T10

Key words: Level set method, phase error, upwinding combined compact scheme, Hamiltonian, symplectic Runge-Kutta, area conservation property.

---

*Corresponding author. *Email address:* twhsheu@ntu.edu.tw (T. W. H. Sheu)

1   Introduction

Along the interface between different phases, surface tension becomes essential in affecting manufacture processes of etching, deposition, lithography, image processing and crystal growth [1]. Studies of these complex phenomena in air-water interfacial dynamics, breaking surface wave, solidification-melt dynamics, two-phase reacting flow, and flow-structure interaction involve getting the temporal surface advancement driven by the carrier flow at different physical loadings. The necessity of capturing or tracking the time-evolving interface with possible sharply-varying surface topology and front propagation speed can make the simulation of differential equations governing their respective two-phase fluid flows an even challenging topic.

Several popular methods such as the vortex method [2], boundary integral method [3], volume of fluid (VOF) method [4], front tracking method [5], and phase field method [6–8] have been successfully applied to predict the air/water interface. One can also combine the level set and projection methods to avoid explicitly tracking the interface [9]. There exist some advantages and disadvantages of applying these interface capturing methods and one is difficult to distinguish which method is superior to the others. ALE (Arbitrary Lagrangian Eulerian) [10] and MAC (Marker and Cell) [11] methods are the two commonly applied interface tracking methods which have been known to be very efficient in modeling a small interface deformation. For an interface undergoing a large deformation, a fairly expensive re-meshing procedure is needed. As the surface tension needs to be considered in the simulation of incompressible two-phase flows, the volume of fluid and level set methods turn out to be more commonly referred to. The VOF method, which is normally represented by a color function, has the ability of conserving the volume of each fluid phase more exactly.

After the pioneering work of Osher and Sethian [12], progress towards refining the level set formulations has made this method a good candidate to simulate the flow problems that involve moving interfaces. Given a smooth level set function for the interface, both interface and its curvature can be easily transported and accurately calculated, respectively. Choice of a proper signed distance function for the sake of re-shaping level set function and implementing a re-initialization procedure for the purpose of enhancing numerical stability are normally required in the level set methods [13]. There is no guarantee that re-initialization process can preserve flow volume or area in time. In each time step, fluid mass of a small quantity may, therefore, be lost or gained. To overcome the problem resulting from the application of level set methods, the particle level set method [14], level set method with mass correction procedure [15], coupled level set and volume of fluid method [16], and adaptive tree method [17] have been proposed. One can refer to the excellent review books of Osher and Fedkiw [18] and Sethian [19] for the details of level set methods. Conservative level set method with the built-in conservative property will be developed in the current incompressible flow simulation to preserve fluid mass [20, 21].

In this paper, we present an upwinding combined compact difference (UCCD) scheme

with minimized phase error that can be used to reduce dispersion error generated from the discrepancy between the effective and actual scaled wave numbers. This scheme can preserve interface shape excellently for the advection equation and helps, thus, the re-initialization process to avoid mass imbalance that is either lost or gained. This paper is organized as follows. Section 2 describes the smoothing method for the two phase flow system which couples the Navier-Stokes equations with the level set method. In Section 3, the incompressible two-phase flow solver carried out in non-staggered grids is presented. The UCCD scheme accommodating the optimized phase property will be employed to calculate the first- and second-order derivative terms simultaneously. In Section 4, the optimized UCCD scheme will be employed to advect interface. In the first step of the level set method, the symplectic-type temporal scheme is applied to solve the pure advection equation. In addition, the re-initialization procedure used for retaining mass conservation in the level set method is presented. Section 5 is presented to justify the analysis code by solving the pure advection equation subjected to a sharply varying initial condition. Section 6 presents the predicted results for the dam-break, Rayleigh-Taylor instability, two-bubble rising, and droplet falling problems. Finally, we will draw some conclusions in Section 7.

2　Mathematical model

For the two immiscible fluids under current investigation, the liquid and gas are both assumed to be incompressible. The resulting equations of motion for these fluids can be represented by the following dimensionless incompressible Navier-Stokes equations:

$$\underline{u}_t + (\underline{u} \cdot \nabla)\underline{u} = \frac{1}{\rho(\phi)}\left(-\nabla p + \frac{1}{Re}\nabla \cdot \left[\mu(\phi)(\nabla\underline{u} + \nabla\underline{u}^{\mathrm{T}})\right] - \frac{1}{We}\delta(\phi)\kappa(\phi)\nabla\phi\right) - \frac{1}{Fr^2}, \quad (2.1a)$$

$$\nabla \cdot \underline{u} = 0. \quad (2.1b)$$

Eq. (2.1a) involves the Dirac delta function δ, level set function ϕ, and three dimensionless parameters, which are known as the Reynolds number $Re = \rho_r U_r L_r / \mu_r$. Froude number $Fr = U_r / \sqrt{gL_r}$, and Weber number $We = \rho_r U_r^2 L_r / \sigma$. In the above, σ is denoted as the surface tension coefficient and U_r, L_r, ρ_r, μ_r are the referenced values for the respective velocity, length, density and viscosity. In addition, two physical properties $\rho(\phi)$ and $\mu(\phi)$ defined as the function of level set function represent the fluid density and viscosity, respectively. The curvature of the time-evolving interface shown in Eq. (2.1a) is denoted as $\kappa = \nabla \cdot (\nabla\phi / |\nabla\phi|)$.

　　The air/water interface, denoted by the chosen level set function ϕ, will be advected in a fluid flow by the linear advection equation given by

$$\phi_t + \underline{u} \cdot \nabla\phi = 0. \quad (2.2)$$

As is usual, the level set function ϕ is initially assigned to have the following signed

distance values

$$
\phi = \begin{cases} -d, & \text{for } x \in \Omega_{gas}, \\ 0, & \text{for } x \in \Gamma_{free\ surface}, \\ d, & \text{for } x \in \Omega_{liquid}. \end{cases} \tag{2.3}
$$

In the above, d denotes the absolute normal distance to the interface.

For the two investigated immiscible fluids, ρ and μ are assumed to be uniform all the time in their respective phases, implying that $D\rho/Dt = D\mu/Dt = 0$. In other words, the transport equations for the fluid density and viscosity depend only on the flow velocity $\underline{u}$ by means of the transport equations given by $\rho_t + (\underline{u} \cdot \nabla)\rho = 0$ and $\mu_t + (\underline{u} \cdot \nabla)\mu = 0$. Across an interface there exist, however, jump conditions for ρ and μ. To prevent numerical instabilities near the interface, we introduce a smoothed Heaviside function given below

$$
H(\phi) = \begin{cases} 0, & \text{if } \phi < -\varepsilon, \\ \dfrac{1}{2}\Big[1 + \dfrac{\phi}{\varepsilon} + \dfrac{1}{\pi}\sin\Big(\dfrac{\pi\phi}{\varepsilon}\Big)\Big], & \text{if } |\phi| \le \varepsilon, \\ 1, & \text{if } \phi > \varepsilon. \end{cases} \tag{2.4}
$$

Choice of this function helps to smoothen out the sharp changes of density and viscosity profiles in the transition zone defined by $|\phi| \le \varepsilon$, where ε, known as the half-thickness of interface, is typically prescribed by the value of Δx or $2\Delta x$. Given the above smoothing function, both of the fluid density and viscosity will be smoothly approximated as

$$
\rho(\phi) = H(\phi) + \Big(\frac{\rho_g}{\rho_l}\Big)(1 - H(\phi)) \quad \text{and} \quad \mu(\phi) = H(\phi) + \Big(\frac{\mu_g}{\mu_l}\Big)(1 - H(\phi)).
$$

Over each time step Δt, ϕ will be firstly computed from the pure advection equation (2.2), which is normally employed to advect the level set function ϕ. The computed solution of ϕ from this equation is then employed as the initial data to solve the following re-initialization equation so as to keep ϕ as the distance function. This procedure ensures that the front of interface has a finite thickness for all time

$$
\phi_t + \text{sgn}(\phi_0)(|\nabla\phi| - 1) = \lambda\delta(\phi)|\nabla\phi|. \tag{2.5}
$$

In the above, $\text{sgn}(\phi_0) = 2(H(\phi_0) - 0.5)$ and the Dirac delta function $\delta(\phi)$ given below is obtained from the $\frac{dH(\phi)}{d\phi}$, which $H(\phi)$ is the smoothed Heaviside function

$$
\delta(\phi) = \frac{dH(\phi)}{d\phi} = \begin{cases} 0, & \text{if } |\phi| > \varepsilon, \\ \dfrac{1}{2\varepsilon}\Big[1 + \cos\Big(\dfrac{\pi\phi}{\varepsilon}\Big)\Big], & \text{if } |\phi| \le \varepsilon. \end{cases} \tag{2.6}
$$

In this study, the magnitude of ε is chosen to be $2\Delta x$ in all calculations. To preserve the area enclosed by the fluid interface, λ shown in Eq. (2.5) is prescribed as [18]

$$
\lambda = -\frac{\int_{\Omega_{i,j}} \delta(\phi)(-\text{sgn}(\phi_0)(|\nabla\phi| - 1))d\Omega}{\int_{\Omega_{i,j}} \delta(\phi)^2|\nabla\phi|d\Omega}. \tag{2.7}
$$

3 Incompressible flow solver in non-staggered grids

3.1 Optimized coupled compact scheme using Lagrange multipliers

Our strategy of approximating the spatial derivative terms shown in the momentum equations follows the work of Chu and Fan [22] to calculate the first- and second-order derivative terms simultaneously. Since the resulting scheme turns out to be more accurate than the conventional finite difference schemes using the same number of stencil points, we are motivated to couple the compact expressions for the first-order and second-order derivative terms. The way of determining the relationship between the two compact representations is to conduct the modified equation analysis, which involves performing a truncated Taylor series, together with the Fourier transform analysis [23], which enables us to get the same or almost the same scaled wavenumber as the original differential equation, in the approximation of convective and diffusive terms.

In what follows, we take the field variable $\phi = u$ (or v) as an example to describe the coupled compact scheme developed in a three-point grid stencil. We assume that the derivative terms $\partial\phi/\partial x$ and $\partial^2\phi/\partial x^2$ will be approximated respectively as follows

$$a_1 \frac{\partial\phi}{\partial x}\Big|_{i-1} + \frac{\partial\phi}{\partial x}\Big|_i = \frac{1}{h}(c_1\phi_{i-1} + c_2\phi_i + c_3\phi_{i+1}) - h\left(b_1 \frac{\partial^2\phi}{\partial x^2}\Big|_{i-1} + b_2 \frac{\partial^2\phi}{\partial x^2}\Big|_i + b_3 \frac{\partial^2\phi}{\partial x^2}\Big|_{i+1}\right), \quad (3.1a)$$

$$\bar{b}_1 \frac{\partial^2\phi}{\partial x^2}\Big|_{i-1} + \frac{\partial^2\phi}{\partial x^2}\Big|_i + \bar{b}_3 \frac{\partial^2\phi}{\partial x^2}\Big|_{i+1} = \frac{1}{h^2}(\bar{c}_1\phi_{i-1} + \bar{c}_2\phi_i + \bar{c}_3\phi_{i+1})$$

$$- \frac{1}{h}\left(\bar{a}_1 \frac{\partial\phi}{\partial x}\Big|_{i-1} + \bar{a}_2 \frac{\partial\phi}{\partial x}\Big|_i + \bar{a}_3 \frac{\partial\phi}{\partial x}\Big|_{i-1}\right). \quad (3.1b)$$

For the other two terms $\partial\phi/\partial y$ and $\partial^2\phi/\partial y^2$ they can be similarly expressed at the nodal points along the y-direction. Prior to determining the above introduced coefficients, it is worth to point out that the compact schemes for $\partial\phi/\partial x|_i$ and $\partial^2\phi/\partial x^2|_i$ are not independent of each other but are rather strongly coupled through the terms $\partial\phi/\partial x|_{i-1}$, $\partial\phi/\partial x|_i$, $\partial\phi/\partial x|_{i+1}$, $\partial^2\phi/\partial x^2|_{i-1}$, $\partial^2\phi/\partial x^2|_i$, $\partial^2\phi/\partial x^2|_{i+1}$, ϕ_{i-1}, ϕ_i and ϕ_{i+1}. For the sake of description, only the positive velocity case will be described in detail. For the case with a negative velocity component, its derivation can be done in a similar way.

3.1.1 Approximation of second-order spatial derivative term

The derivative term $\partial^2\phi/\partial x^2$ is normally approximated by the central scheme since its discretization error is prevailingly dissipative. For this reason, the weighting coefficients shown in Eq. (3.1b) will be determined solely from the modified equation analysis. Derivation of the coefficients $\bar{a}_1$, $\bar{a}_2$, $\bar{a}_3$, $\bar{b}_1$, $\bar{b}_3$, $\bar{c}_1$, $\bar{c}_2$ and $\bar{a}_3$ in this equation so as to get a higher spatial accuracy is as follows.

We start by expanding ϕ_{i+1}, $\partial\phi/\partial x|_{i+1}$ and $\partial^2\phi/\partial x^2|_{i+1}$ in Taylor series with respect to ϕ_i, $\partial\phi/\partial x|_i$ and $\partial^2\phi/\partial x^2|_i$ and then, eliminating the leading error terms in the modified equation. Elimination of the leading eight error terms enables us to get the following

algebraic equations for Eq. (3.1b), which are

$$\bar{c}_1+\bar{c}_2+\bar{c}_3=0, \qquad\qquad -\bar{a}_1-\bar{a}_2-\bar{a}_3-\bar{c}_1+\bar{c}_3=0,$$

$$\bar{a}_1-\bar{a}_3-\bar{b}_1+\frac{\bar{c}_1}{2}-\bar{b}_3+\frac{\bar{c}_3}{2}-1=0, \qquad -\frac{\bar{a}_1}{2}-\frac{\bar{a}_3}{2}+\bar{b}_1-\bar{b}_3-\frac{\bar{c}_1}{6}+\frac{\bar{c}_3}{6},$$

$$\frac{\bar{a}_1}{6}-\frac{\bar{a}_3}{6}-\frac{\bar{b}_1}{2}+\frac{\bar{c}_1}{24}-\frac{\bar{b}_3}{2}+\frac{\bar{c}_3}{24}=0, \qquad -\frac{\bar{a}_1}{24}-\frac{\bar{a}_3}{24}+\frac{\bar{b}_1}{6}-\frac{\bar{b}_3}{6}-\frac{\bar{c}_1}{120}+\frac{\bar{c}_3}{120}=0,$$

$$\frac{\bar{a}_1}{120}-\frac{\bar{a}_3}{120}-\frac{\bar{b}_1}{24}-\frac{\bar{b}_3}{24}+\frac{\bar{c}_1}{720}+\frac{\bar{c}_2}{720}=0, \qquad -\frac{\bar{a}_1}{720}-\frac{\bar{a}_3}{720}+\frac{\bar{b}_1}{120}-\frac{\bar{b}_3}{120}-\frac{\bar{c}_1}{5040}+\frac{\bar{c}_3}{5040}=0.$$

When solving this set of algebraic equations we can easily get the coefficients in Eq. (3.1b) as $\bar{a}_1=-9/8$, $\bar{a}_2=0$, $\bar{a}_3=9/8$, $\bar{b}_1=-1/8$, $\bar{b}_3=-1/8$, $\bar{c}_1=3$, $\bar{c}_2=-6$, $\bar{c}_3=3$. By virtue of the following derived modified equation, we know that the presently derived set of eight weighting coefficients can be applied to get the spatial accuracy order of sixth for the second-order derivative term

$$\frac{\partial^2\phi}{\partial x^2}=\frac{\partial^2\phi}{\partial x^2}\Big|_{exact}+\frac{h^6}{20160}\frac{\partial^8\phi}{\partial x^8}+\frac{h^8}{604800}\frac{\partial^{10}\phi}{\partial x^{10}}+\mathcal{O}(h^{12})+H.O.T. \tag{3.2}$$

3.1.2 Approximation of first-order spatial derivative term

We will then determine the coefficients a_1, b_1, b_2, b_3, c_1, c_2 and c_3 shown in Eq. (3.1a) by partly applying the Taylor series expansions for $\phi_{i\pm1}$, $\partial\phi/\partial x|_{i\pm1}$ and $\partial^2\phi/\partial x^2|_{i\pm1}$ with respect to ϕ_i, $\partial\phi/\partial x|_{i\pm1}$ and $\partial^2\phi/\partial x^2|_{i\pm1}$. Elimination of the six leading error terms derived in the modified equation enables us to get the following set of algebraic equations

$$c_1+c_2+c_3=0, \qquad\qquad -a_1-c_1+c_3-1=0, \tag{3.3a}$$

$$-a_1+b_1+b_2+b_3-\frac{c_1}{2}-\frac{c_3}{2}=0, \qquad \frac{a_1}{2}-b_1+b_3+\frac{c_1}{6}-\frac{c_3}{6}=0, \tag{3.3b}$$

$$-\frac{a_1}{6}+\frac{b_1}{2}+\frac{b_3}{2}-\frac{c_1}{24}-\frac{c_3}{24}=0, \qquad \frac{a_1}{24}-\frac{b_1}{6}+\frac{b_3}{6}+\frac{c_1}{120}-\frac{c_3}{120}=0. \tag{3.3c}$$

It is now still short of one algebraic equation to uniquely determine all the seven introduced coefficients shown in Eq. (3.1a). For getting an accurate approximation of the first-order derivative term from Eq. (3.1a), one should retain the dispersive nature embedded in $\partial\phi/\partial x$ as much as possible [24].

The expressions of the actual wavenumber for Eqs. (3.1a) and (3.1b) can be derived as

$$i\alpha h(a_1\exp(-i\alpha h)+1)\simeq c_1\exp(-i\alpha h)+c_2+c_3\exp(i\alpha h)$$
$$-(i\alpha h)^2(b_1\exp(-i\alpha h)+b_2+b_3\exp(i\alpha h)), \tag{3.4a}$$

$$i\alpha h\left(-\frac{8}{9}\exp(-i\alpha h)+\frac{8}{9}\exp(i\alpha h)\right)\simeq 3\exp(-i\alpha h)-6+3\exp(i\alpha h)$$
$$-(i\alpha h)^2\left(-\frac{1}{8}\exp(-i\alpha h)+1-\frac{1}{8}\exp(i\alpha h)\right). \tag{3.4b}$$

The chosen strategy of reducing dispersion error for the approximated first-order derivative term is to match the exact wavenumber with the numerical wavenumber. This amounts to equating the effective wavenumbers α' and α'' to those shown in the right-hand sides of Eqs. (3.4a) and (3.4b) (see [24]). We will, as a result, express α' and α'' as follows :

$$i\alpha'h(a_1\exp(-i\alpha h)+1)=c_1\exp(-i\alpha h)+c_2+c_3\exp(i\alpha h)$$
$$-(i\alpha''h)^2(b_1\exp(-i\alpha h)+b_2+b_3\exp(i\alpha h)), \tag{3.5a}$$

$$i\alpha'h\left(-\frac{8}{9}\exp(-i\alpha h)+\frac{8}{9}\exp(i\alpha h)\right)=3\exp(-i\alpha h)-6+3\exp(i\alpha h)$$
$$-(i\alpha''h)^2\left(-\frac{1}{8}\exp(-i\alpha h)+1-\frac{1}{8}\exp(i\alpha h)\right). \tag{3.5b}$$

By solving the above two equations, α and α'' can be derived as follows

$$\alpha'h=-i\Big(24b_1\exp(-2i\alpha h)+c_1\exp(-2i\alpha h)+c_3+c_1+24b_1+c_2\exp(-i\alpha h)$$
$$+24b_2\exp(-i\alpha h)+24b_3-48b_1\exp(-i\alpha h)-8c_1\exp(-i\alpha h)-48b_3\exp(i\alpha h)$$
$$+24b_2\exp(i\alpha h)+24b_3\exp(2i\alpha h)-48b_2+c_2\exp(i\alpha h)+c_3\exp(2i\alpha h)$$
$$-8c_3\exp(i\alpha h)-8c_2\Big)\big(-8+\exp(i\alpha h)-8a_1\exp(-i\alpha h)+a_1\exp(-2i\alpha h)$$
$$-9b_1\exp(-2i\alpha h)-9b_2\exp(-i\alpha h)+9b_2\exp(i\alpha h)+9b_3\exp(2i\alpha h)$$
$$+a_1+9b_1-9b_3+\exp(i\alpha h)\Big)^{-1}, \tag{3.6a}$$

$$\alpha''h=\sqrt{-\frac{3\exp(-i\alpha h)-6+3\exp(i\alpha h)-i\alpha'h\big(-8\exp(-i\alpha h)/9+8\exp(i\alpha h)/9\big)}{-\exp(-i\alpha h)/8+1-\exp(i\alpha h)/8}}. \tag{3.6b}$$

To minimize the dispersion error, the modified wavenumber of the proposed scheme (or $\alpha'h$) is made to equate to αh as much as possible. This implies that the function E defined below should be very small and positive over the chosen range of scaled wavenumber, which is in between $-\pi/2$ and $\pi/2$ (see [24])

$$E=\int_{-\frac{\pi}{2}}^{\frac{\pi}{2}}\big[W(\alpha h-\Re[\alpha'h])\big]^2d(\alpha h)=\int_{-\frac{\pi}{2}}^{\frac{\pi}{2}}\big[W(\gamma-\Re[\gamma'])\big]^2d\gamma. \tag{3.7}$$

In the above, $\Re[\gamma']$ denotes the real part of $\alpha'h$, $\gamma=\alpha h$ and $\gamma'=\alpha'h$. Note that Eq. (3.7) can be analytically integrated provided that the weighting function W shown above is chosen as the denominator of $(\gamma-\Re[\gamma'])$ (see [25]).

$$W=-16+72b_3+72b_1-81b_1^2-81b_3^2-81b_2^2-162b_2b_3\cos(\gamma)-144a_1b_3\cos(\gamma)$$
$$-162b_1b_2\cos(\gamma)-a_1^2\cos(\gamma)^2+8a_1^2\cos(\gamma)-18b_3\cos(\gamma)^3+18b_1\cos(\gamma)^3$$
$$+81b_2^2\cos(\gamma)^2+162b_1b_3-72b_1\cos(\gamma)+81b_3^2\cos(\gamma)^2+81b_1^2\cos(\gamma)^2$$
$$-72a_1b_2-18b_1\cos(\gamma)+16a_1\cos(\gamma)^2-2a_1\cos(\gamma)^3+72b_3\cos(\gamma)^2+18b_3\cos(\gamma)$$
$$-32a_1\cos(\gamma)-36a_1b_3\cos(\gamma)^4-18a_1b_2\cos(\gamma)^3+162b_2b_3\cos(\gamma)^3$$
$$-486b_1b_3\cos(\gamma)^2+36a_1b_3\cos(\gamma)^2+18a_1b_2\cos(\gamma)+8\cos(\gamma)-16a_1^2-\cos(\gamma)^2. \tag{3.8}$$

For the determination of the unknown coefficients a_1, b_1 to b_3 and c_1 to c_3, we will minimize E by the method of Lagrange multipliers, which is considered as a rigorous analytic means of finding the extrema of a function subject to the six constraint equations shown in (3.3a)-(3.3c). A proper determination of these coefficients should, as a result, take all the six constraint equations into consideration. The above two requirements prompt us to minimize the following function G, which is called as the Lagrange function, subject to the constraints given in (3.3a)-(3.3c)

$$
\begin{aligned}
G&(a_1,b_1,b_2,b_3,c_1,c_2,c_3)\\
=&E+\lambda_1\cdot(c_1+c_2+c_3)+\lambda\cdot(-a_1-c_1+c_3-1)\\
&+\lambda_3\cdot\left(-a_1+b_1+b_2+b_3-\frac{c_1}{2}-\frac{c_3}{2}\right)+\lambda_4\cdot\left(\frac{a_1}{2}-b_1+b_3+\frac{c_1}{6}-\frac{c_3}{6}\right)\\
&+\lambda_5\cdot\left(-\frac{a_1}{6}+\frac{b_1}{2}+\frac{b_3}{2}-\frac{c_1}{24}-\frac{c_3}{24}\right)+\lambda_6\cdot\left(\frac{a_1}{24}-\frac{b_1}{6}+\frac{b_3}{6}+\frac{c_1}{120}-\frac{c_3}{120}\right).
\end{aligned}
\tag{3.9}
$$

In the above, λ_1 to λ_6 are known as the Lagrange multipliers and they will be determined later on.

By performing $\partial G/\partial\lambda_i=0$ $(i=1,2,3,4,5,6)$, one can re-derive the algebraic equations shown in (3.3a)-(3.3c). To minimize the Lagrange function G of seven variables, we perform

$$
\frac{\partial G}{\partial a_1}=\frac{\partial G}{\partial b_1}=\frac{\partial G}{\partial b_2}=\frac{\partial G}{\partial b_3}=\frac{\partial G}{\partial c_1}=\frac{\partial G}{\partial c_3}=0
$$

to get six algebraic equations, from which one can uniquely determine the Lagrange multipliers λ_1 to λ_6. Since the derived expressions of these Lagrange multipliers, which are expressed as the functions of a_1, b_1 to b_3 and c_1 to c_3 are fairly lengthy, they will not be given in this paper for saving the space. Derivation of the coefficients in the proposed combined compact scheme is followed by performing

$$
\frac{\partial G}{\partial c_2}\equiv G_d(a_1,b_1,b_2,b_3,c_1,c_2,c_3)=0
$$

and then substituting the Lagrangian multipliers λ_1 to λ_6 to the resulting equation $G_d=0$ to yield an algebraic equation, which involves coefficients a_1, b_1 to b_3, and c_1 to c_3. According Eqs. (3.3a)-(3.3c), we can rewrite a_1, b_1 to b_3, c_1 and c_3 in terms of c_2 as follows:

$$
a_1=\frac{7}{8}, \qquad\qquad b_1=\frac{5}{24}-\frac{1}{24}c_2, \qquad\qquad b_2=\frac{7}{12}-\frac{5}{12}c_2,
$$
$$
b_3=\frac{1}{12}-\frac{1}{24}c_2, \qquad c_1=-\frac{1}{2}c_2-\frac{15}{16}, \qquad c_3=\frac{15}{16}-\frac{1}{2}c_2.
$$

Note that the nodal point numbered by the subscript 2 is the reference node chosen for the approximation of ϕ_x in (3.1a). At this moment, one can get the final required algebraic

equation $G_d(c_2) = 0$, which is given below

$$\left(-\frac{63994136561}{823200} + \frac{539508989}{32768}\pi + \frac{2203629}{1792}\pi^2 + \frac{7334019}{16384}\pi^3\right)c_2$$

$$+ \left(\frac{31233753}{980} - \frac{1824908967}{262144}\pi - \frac{14337}{32}\pi^2 - \frac{5897367}{32768}\pi^3\right)c_2^2$$

$$- \left(\frac{31233753}{6860} - \frac{260701281}{262144}\pi - \frac{14337}{224}\pi^2 - \frac{842481}{32768}\pi^3\right)c_2^3$$

$$+ \frac{23182032641}{352800} - \frac{5170636205}{393216}\pi - \frac{318239}{256}\pi^2 - \frac{3205041}{8192}\pi^3 = 0. \tag{3.10}$$

We can then solve the above equation to get its three roots, which are $c_2 = 2.333333$, 1.997587 and 2.669080. By substituting these roots into Eq. (3.9), one knows from Fig. 1 that G indeed has its smaller local minimum $(0.905180 \times 10^{-18})$ at $c_2 = 1.997587$. Now, we can further substitute c_2 into

$$(a_1, b_1, b_2, b_3, c_1, c_3) = \left(\frac{7}{8}, \frac{5}{24} - \frac{1}{24}c_2, \frac{7}{12} - \frac{5}{12}c_2, \frac{1}{12} - \frac{1}{24}c_2, -\frac{1}{2}c_2 - \frac{15}{16}, \frac{15}{16} - \frac{1}{2}c_2\right)$$

to uniquely determine the coefficients as

$$a_1 = 0.875, \qquad b_1 = 0.125128, \qquad b_2 = -0.248718, \qquad b_3 = 0.000128, \tag{3.11}$$

$$c_1 = -1.935961, \qquad c_2 = 1.996922, \qquad c_3 = -0.060961. \tag{3.12}$$

From the resulting derived modified equation for ϕ_x, we know that the spatial accuracy order is fifth since the discretization error E_{rr} can be derived as follows for the first-order derivative term $\partial\phi/\partial x$

$$E_{rr} = 0.000700\frac{\partial^6\phi}{\partial x^6}h^5 + 0.000198\frac{\partial^7\phi}{\partial x^7}h^6 + H.O.T. \tag{3.13}$$

At the two boundary points at x_1 and x_n the following fourth-order accurate one-sided boundary combined compact schemes can be similarly derived in a stencil of three grid points:

$$\phi_1' + 2\phi_2' - h\phi_2'' = \frac{1}{h}(-3.5\phi_1 + 4\phi_2 - 0.5\phi_3), \tag{3.14a}$$

$$h\phi_1'' + 5h\phi_2'' - 6\phi_2' = \frac{1}{h}(9\phi_1 - 12\phi_2 + 3\phi_3), \tag{3.14b}$$

$$\phi_N' + 2\phi_{N-1}' + h\phi_{N-1}'' = \frac{1}{h}(3.5\phi_N - 4\phi_{N-1} + 0.5\phi_{N-2}), \tag{3.14c}$$

$$h\phi_N'' + 5h\phi_{N-1}'' + 6\phi_{N-1}' = \frac{1}{h}(9\phi_N - 12\phi_{N-1} + 3\phi_{N-2}). \tag{3.14d}$$

The proposed three-point upwind combined compact scheme, which consists of Eqs. (3.14a) and (3.14b) for the node at $i = 1$, Eqs. (3.14c) and (3.14d) for the node at $i = N$ and Eqs. (3.1a) and (3.1b) derived at the nodal points $i = 2, 3, 4, 5, \cdots, N-1$, formulates a $2N \times 2N$ matrix system, which can be effectively solved by the twin-tridiagonal solution solver [22].
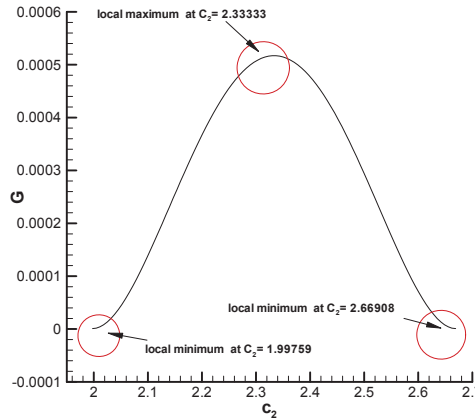
Figure 1: The Lagrange function $G(c_2)$, defined in (3.9), plotted against c_2 for showing its local maximum and minimum.

3.2 Compact scheme for the pressure gradient in collocated grids

For the sake of programming simplicity and parallelization, Eqs. (2.1a)-(2.1b) will be solved in non-staggered (or collocated) grids. When approximating the primitive-variable incompressible viscous flow equations in non-staggered grids, it is essential to get rid of the even-odd spurious pressure oscillations. Elimination of these unphysical oscillatory solutions motivated us to calculate the pressure gradient term, say for example at an interior grid point (i,j), from the following equation

$$e_1 F_{i+1,j} + e_2 F_{i,j} + e_3 F_{i-1,j} = e_4 (p_{i+2,j} - p_{i+1,j}) + e_5 (p_{i+1,j} - p_{i,j})$$
$$+ e_6 (p_{i,j} - p_{i-1,j}) + e_7 (p_{i-1,j} - p_{i-2,j}), \tag{3.15}$$

where $F_{i,j} = h \partial p / \partial x |_{i,j}$. To start with, Taylor series expansions for $F_{i\pm1,j}$, $p_{i\pm1,j}$ and $p_{i\pm2,j}$ are performed with respect to $F_{i,j}$, $p_{i,j}$, respectively. This is followed by substituting the resulting Taylor series expansion equations into Eq. (3.15) to get $e_1 = 1/5$, $e_2 = 3/5$, $e_3 = 1/5$, $e_4 = 1/60$, $e_5 = e_6 = 29/60$ and $e_7 = 1/60$. As for the approximation of $\partial p / \partial y$, it can be similarly done using the above compact approximation method.

3.3 Divergence-free-condition compensated solution algorithm for two phase flow

Following the idea of projection method, we can use the predicted pressure p^* to calculate the intermediate velocity u^*, which does not satisfy the divergence-free constraint condition, from the following momentum vector equation

$$\frac{\overline{u}^* + \overline{u}^n}{\Delta t} + (\overline{u}^* \cdot \nabla) \overline{u}^* - \frac{1}{\rho(\phi) Re} \nabla \cdot \mu(\phi) \nabla u^* + \frac{\nabla p^*}{\rho(\phi)} = \underline{f}. \tag{3.16}$$

The velocity is then projected to the divergence-free space to update the pressure magnitude as

$$\frac{\underline{u}^{n+1}-\underline{u}^n}{\Delta t}=-\frac{\nabla p'}{\rho(\phi)},\tag{3.17a}$$

$$p^{n+1}=p^*+p',\tag{3.17b}$$

$$\nabla\cdot\underline{u}^{n+1}=0.\tag{3.17c}$$

Substitution of Eq. (3.17a) to the semi-discrete equation

$$\frac{\underline{u}^{n+1}-\underline{u}^n}{\Delta t}+(\underline{u}^{n+1}\cdot\nabla)u^{n+1}-\frac{1}{\rho(\phi)Re}\nabla\cdot\mu(\phi)\nabla\underline{u}^{n+1}+\frac{\nabla p^{n+1}}{\rho(\phi)}=\underline{f}$$

yields [26]

$$\frac{\underline{u}^{n+1}-\underline{u}^n}{\Delta t}+(\underline{u}^*\cdot\nabla)u^*-\frac{1}{\rho(\phi)Re}\nabla\cdot\mu(\phi)\nabla\underline{u}^*+\frac{\nabla p^*}{\rho(\phi)}=-\frac{\nabla p'}{\rho(\phi)}+\underline{f}+M_1+M_2,\tag{3.18}$$

where

$$M_1=\left[(\underline{u}^*\cdot\nabla)\frac{\nabla p'}{\rho(\phi)}+\left(\frac{\nabla p'}{\rho(\phi)}\cdot\nabla\right)\underline{u}^*\right]\Delta t-\frac{1}{\rho(\phi)Re}\nabla(\nabla\cdot\underline{u}^*),\tag{3.19a}$$

$$M_2=-\left[\left(\frac{\nabla p'}{\rho(\phi)}\cdot\nabla\right)\frac{\nabla p'}{\rho(\phi)}\right]\Delta t^2,\tag{3.19b}$$

$$p'_{i,j}=p'^{*}_{i,j}+\frac{\left(\frac{1}{\rho_{i+\frac{1}{2},j}}\Delta x^2+\frac{1}{\rho_{i-\frac{1}{2},j}}\Delta x^2+\frac{1}{\rho_{i,j+\frac{1}{2}}}\Delta y^2+\frac{1}{\rho_{i,j-\frac{1}{2}}}\Delta y^2\right)}{\left(\frac{p'^{*}_{i+1,j}}{\rho_{i+\frac{1}{2},j}}\Delta x^2+\frac{p'^{*}_{i-1,j}}{\rho_{i-\frac{1}{2},j}}\Delta x^2+\frac{p'^{*}_{i,j+1}}{\rho_{i,j+\frac{1}{2}}}\Delta y^2+\frac{p'^{*}_{i,j-1}}{\rho_{i,j-\frac{1}{2}}}\Delta y^2\right)}.\tag{3.19c}$$

The computational procedures of the proposed Level Set (LS) method, combined with the DFC (Divergence Free Compensated) method (LS-DFC), are summarized as follows:

Given the predicted values of u_0^* and p_0^* for $s=0,1,2,\cdots$,

(I) Calculate the intermediate velocity $\underline{u}_s^{n+1}$ by solving the following momentum equations in the fluid-domain

$$\frac{\underline{u}_s^{n+1}-\underline{u}^n}{\Delta t}+\underline{u}_s^*\cdot\nabla\underline{u}_s^*-\frac{1}{\rho(\phi)Re}\nabla\cdot\mu(\phi)\nabla\underline{u}_s^*=-\frac{\nabla p^*_{s-1}}{\rho(\phi)}+\underline{f}_{s-1}+M_{DFC_{s-1}}.\tag{3.20}$$

(II) Calculate p_s^* and u_{s+1}^* by

$$p_s^*=p_{s-1}^*+p'_s,\tag{3.21a}$$

$$\underline{u}_{s+1}^*=\underline{u}_s^{n+1}.\tag{3.21b}$$

(III) When convergence is reached, set $\underline{u}_{s+1}^{n+1}=\underline{u}^{n+1}$ and $p_s^*=p^{n+1}$ and goto the next time step; else go to (I).

4 Level set equation solver

Eq. (2.2) is known to have the following Hamiltonian [27]

$$H = \frac{1}{2} \int_{\Omega} \psi \phi \, d\Omega, \tag{4.1}$$

where ψ denotes the streamfunction governed by $u = \partial\psi/\partial y$ and $v = -\partial\psi/\psi x$. Employment of a scheme which accommodates the above Hamiltonian property is essential in the interface prediction using the level set method [28]. For the purpose of preserving the long-term accurate Hamiltonian property embedded in Eq. (2.2), the time derivative term will be discretized by the symplectic scheme. In this paper, the following sixth-order temporally accurate symplectic Runge-Kutta scheme [29] will be employed to solve the ordinary differential equation.

With the computed time accurate solution ϕ^n at $t = n\Delta t$, we will calculate ϕ^{n+1} by using the following iterative method. We start with the guessed values $\phi^{(i)}$ for ϕ^n, where $i = 1$ to 3, and then calculate the values of $F^{(i)}$ ($\equiv -\underline{u}\nabla\phi^{(i)}$). This is followed by substituting $F^{(i)}$ ($i=1$ to 3) into the following three equations to get the updated values of $\phi^{(i)}$ ($i=1$ to 3).

$$\phi^{(1)} = \phi^n + \Delta t \left[\frac{5}{36} F^{(1)} + \left(\frac{2}{9} + \frac{2\tilde{c}}{3} \right) F^{(2)} + \left(\frac{5}{36} + \frac{\tilde{c}}{3} \right) F^{(3)} \right], \tag{4.2a}$$

$$\phi^{(2)} = \phi^n + \Delta t \left[\left(\frac{5}{36} - \frac{5\tilde{c}}{12} \right) F^{(1)} + \frac{2}{9} F^{(2)} + \left(\frac{5}{36} + \frac{5\tilde{c}}{12} \right) F^{(3)} \right], \tag{4.2b}$$

$$\phi^{(3)} = \phi^n + \Delta t \left[\left(\frac{5}{36} - \frac{\tilde{c}}{3} \right) F^{(1)} + \left(\frac{2}{9} - \frac{2\tilde{c}}{3} \right) F^{(2)} + \frac{5}{36} F^{(3)} \right], \tag{4.2c}$$

where $\tilde{c} = \sqrt{3/5}/2$. Note that $F^{(i)}$ ($i=1$ to 3), which are shown in the right hand side of Eq. (2.2), represent the values of F evaluated respectively at $t = n + (0.5 + \tilde{c})\Delta t$, $t = n + 0.5\Delta t$, $t = n + (0.5 - \tilde{c})\Delta t$. Unless the computed difference of $\phi^{(i)}$ between two consecutive iterations becomes a negligibly small value, we continue the calculation of $F^{(i)}$ according to Eqs. (4.2a)-(4.2c). Upon reaching the user specified tolerance, we can compute the solution at $t = (n+1)\Delta t$ from the following equation:

$$\phi^{n+1} = \phi^n + \Delta t \left[\frac{5}{18} F^{(1)} + \frac{4}{9} F^{(2)} + \frac{5}{18} F^{(3)} \right]. \tag{4.3}$$

5 Verification and comparison studies

For the sake of assessment, the proposed combined compact scheme with the minimized phase error will be compared with other previously proposed fifth-order and sixth-order accurate schemes. These chosen comparison schemes are summarized below.

(I) Fifth-order accurate optimized upwind compact scheme (OUC) [30]

$$
\begin{aligned}
25\frac{\partial \phi}{\partial x}\Big|_{i-1} &+ 60\frac{\partial \phi}{\partial x}\Big|_{i} + 15\frac{\partial \phi}{\partial x}\Big|_{i+1} \\
&= \frac{1}{h}\left(-\frac{5}{2}\phi_{i-2} - \frac{160}{3}\phi_{i-1} + 15\phi_i + 40\phi_{i+1} + \frac{5}{6}\phi_{i+2}\right).
\end{aligned}
\tag{5.1}
$$

(II) Sixth-order accurate Wave Number Extended explicit scheme (WNE) [31]

$$
\begin{aligned}
\frac{\partial \phi}{\partial x}\Big|_i = \frac{1}{h}\big[&0.015825\phi_{i-4} - 0.127442\phi_{i-3} + 0.482326\phi_{i-2} - 1.303877\phi_{i-1} \\
&+ 0.553877\phi_i + 0.417674\phi_{i+1} - 0.039225\phi_{i+2} + 0.000842\phi_{i+3}\big].
\end{aligned}
\tag{5.2}
$$

(III) Fifth-order accurate upwind scheme (5U)

$$
\frac{\partial \phi}{\partial x}\Big|_i = \frac{1}{h}\left[-\frac{1}{30}\phi_{i-3} + \frac{1}{4}\phi_{i-2} - \phi_{i-1} + \frac{1}{3}\phi_i + \frac{1}{2}\phi_{i+1} - \frac{1}{20}\phi_{i+2}\right].
\tag{5.3}
$$

In addition, we define below the computed error cast in its percentage form by

$$
Error_A = \frac{A(t) - A(t=0)}{A(t=0)} \times 100\%,
\tag{5.4}
$$

where $A(t) = \int_\Omega H(\phi)d\Omega$.

5.1 Vortex flow in a box

The vortex problem of Wusi et al. [32] will be investigated in a square domain, within which the velocity field (u,v) is given by $u = -\sin^2(\pi x/100)\sin(\pi y/50)$ and $v = \sin^2(\pi y/100)\sin(\pi x/50)$. The circle initially centered at $(50,75)$ has a radius of 15. This test problem will be solved at $\Delta t = 0.01\Delta x$ in a domain of 100×100 and 200×200 grids. The predicted results at $t = 400$ in the two chosen grids (in Fig. 2 and Fig. 3, respectively) are seen to get distorted from the initial solution and form a long filamentary shape by the specified stretching and tearing flow field. In addition, the area error $Error_A$ defined in (5.4) is plotted in the two chosen grids in Fig. 4 to show the area preserving property.

5.2 Rotation of a Zalesak's slotted disk

The Zalesak's problem, which simulates the rotating slotted disk [33], has become the best known benchmark case for testing the advection scheme. The sharp profile of a notched disc type with the slot width of 15 is rotated about the point at $(50,75)$ in an inviscid flow with the velocity field given by

$$
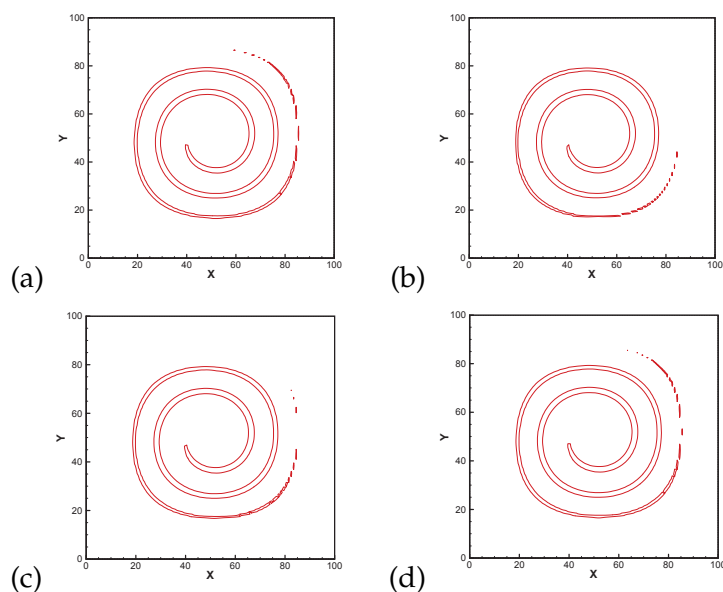(u,v) = \left(\frac{\pi(50-y)}{314}, \frac{\pi(x-50)}{314}\right).
$$

Figure 2: Vortex flow in a box: the predicted interfaces in a domain of 100×100 grids. (a) present; (b) 5U; (c) WNE [31]; (d) OUC [30].
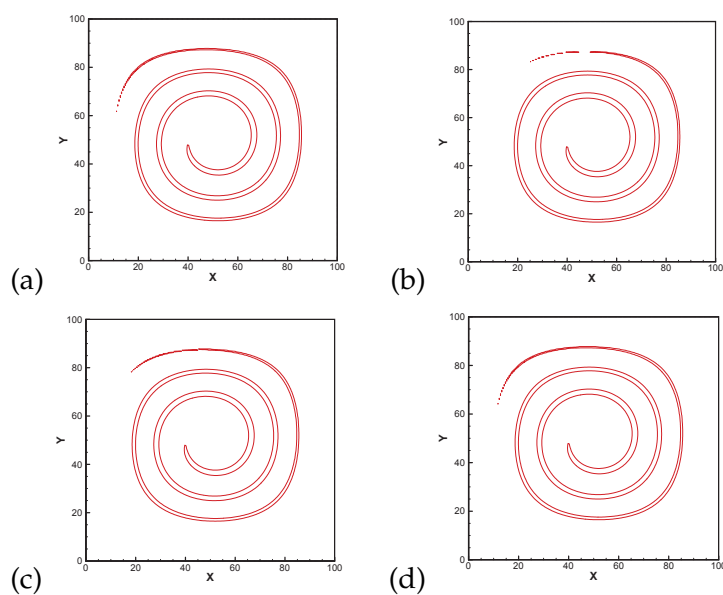

Figure 3: Same as Fig. 2, except with 200×200 grids.

Calculation will be carried out in 100×100 grids to get the solution at the time after fifteen revolutions. Our computed solution shown in Fig. 5 was seen to be in good agreement with the exact (or initial) solution in view of the computed smaller area error $Error_A$
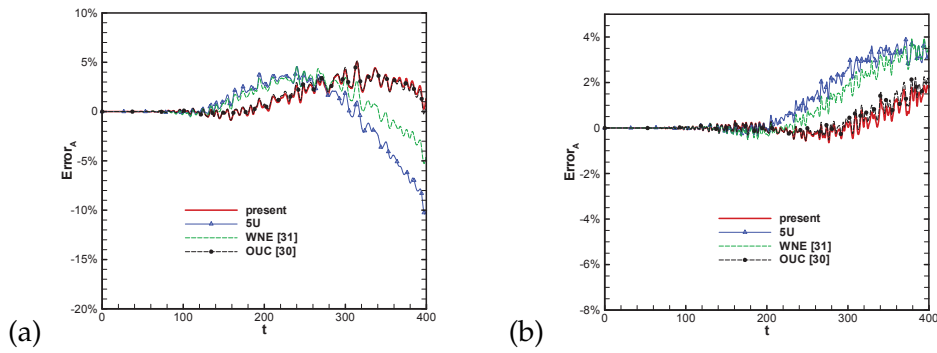
(a)   (b)

Figure 4: Vortex flow in a box: the area errors, defined in (5.4), plotted against the time. (a) $\Delta x = \Delta y = 1$; (b) $\Delta x = \Delta y = 1/2$.

(a)   (b)

(c)   (d)
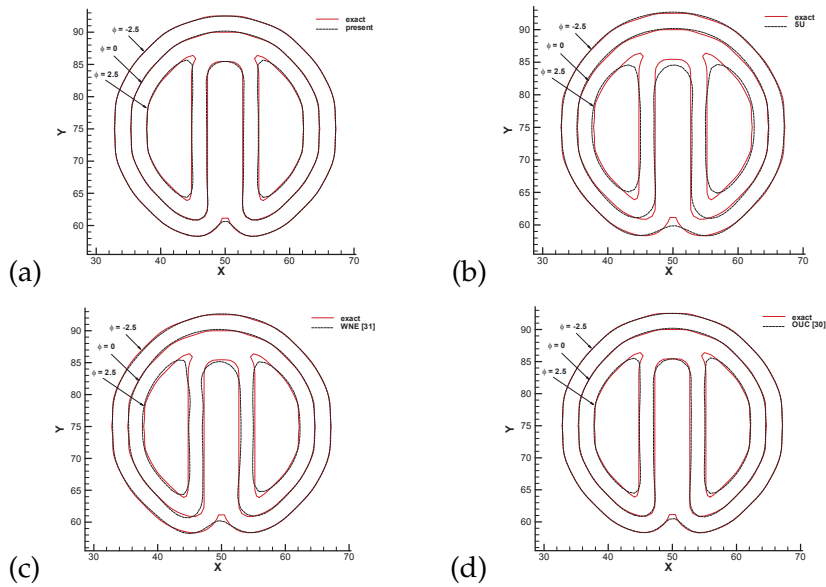
Figure 5: Rotation of a Zalesak's slotted disk: the predicted interfaces with 100×100 grids. (a) present; (b) 5U; (c) WNE [31]; (d) OUC [30].
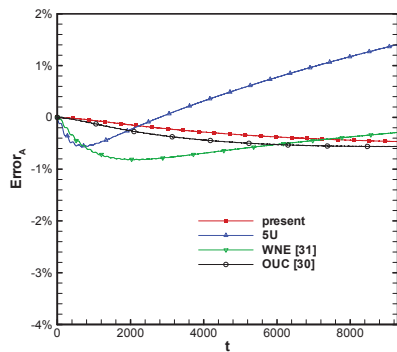
Figure 6: Rotation of a Zalesak's slotted disk: the area errors, defined in (5.4), plotted against the time t using four schemes.
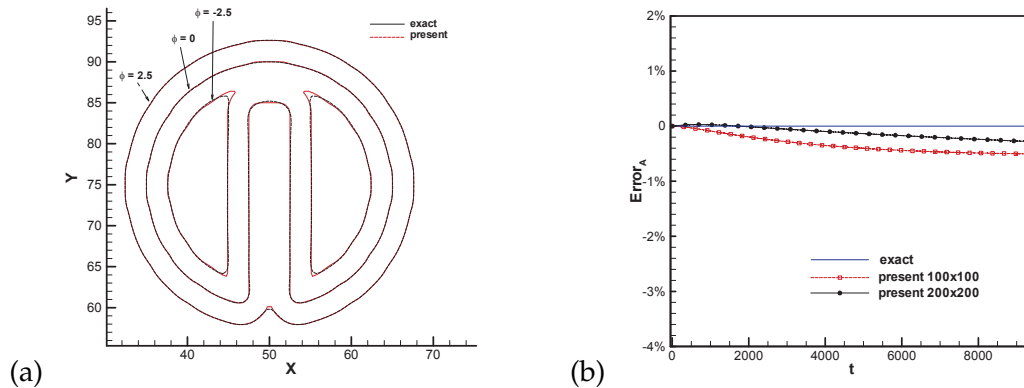
Figure 7: (a) The interfaces predicted from four schemes with 200×200 grids; (b) The predicted area errors plotted against the time t in the two chosen grids.

shown in Fig. 6. In addition, the improved results computed by the current scheme in the domain containing 200×200 nodal points can be clearly seen in Fig. 7, which plots the solutions at the time after fifteen revolutions.

6   Numerical results

After verifying the advection scheme, we will proceed to justify the proposed level set method by virtue of the following four problems, which all involve predicting the time-varying interface shapes.

6.1   Interface prediction without surface tension

6.1.1   Dam break problem

Water column collapsed to a rigid horizontal wall has been frequently investigated to validate the computer code developed for the prediction of free surface. In addition to the hydraulic importance in this dam break problem, the experimental data given in [34] are available for us to properly make a direct comparison study. The computational domain is 5×1.25, which is sketched in Fig. 8. In a uniform grid of 400×100 mesh points, the results will be predicted at $Re = 42792$. Good agreement with the experimental result given in [34] is clearly demonstrated in Fig. 9 for the predicted surge front location and the water column height.

The time-evolving surface position and stream function are plotted in Fig. 10. In Fig. 10(g), the surge front is seen to reflect from the right wall and fall into the bottom water pool. An elongated thin surge is, thus, created by the splashing of the surge front in Fig. 10(i). For an indirect verification of the predicted results, the time history of the area will be plotted in 200×50 and 300×75 nodal points in Fig. 11. One can fairly say
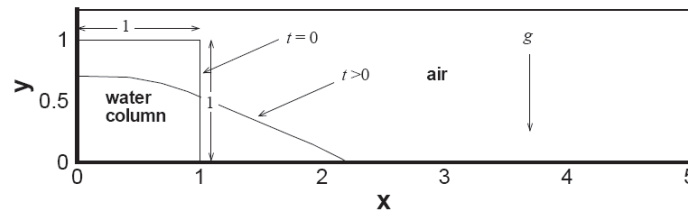
Figure 8: Schematic of the dam break problem considered in Section 6.1.1.
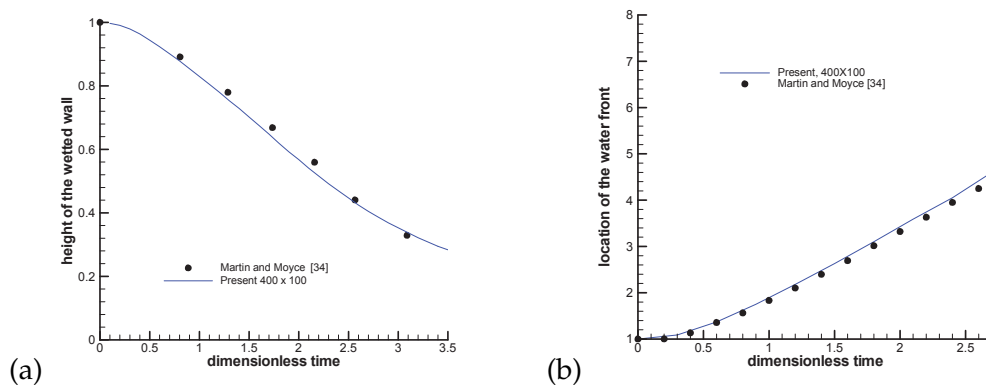

Figure 9: Comparison of the predicted surge front location and the water column height with the experimental data. (a) Height of the wetted wall; (b) location of the water front.

that the area is conserved quite well for the case with a fast-transient surface motion and a large topological change of the free surface. In addition, the effect with/without re-initialization correction procedure is investigated. The necessity of performing re-initialization correction procedure is clearly confirmed from the three predicted sets of results, computed in the 300×75 mesh, which are plotted in Fig. 11. It is also worthy to point out here that the area preservation ability embedded in the pure advection scheme helps to reduce much of the computational time since the required number of re-initialization steps decreases considerably. For clearly showing the save of CPU times, we tabulate them in Table 1 for the calculation running on a personal computer with Intel i7-930.

Table 1: Comparison of CPU times for the four test problems solved at $\Delta t = 10^{-2} \Delta x$ for the calculations carried out in between $0 \leq t \leq T$.

	No. of mesh points	T	CPU times	
			Conventional level set method	Current level set method
Dam-break problem	400×100	3s	8795s	5051s
Rayleigh-Taylor problem	100×400	2.5s	9710s	4777s
Two-bubble rising problem	140×280	2.5s	22550s	18124s
Droplet falling problem	140×210	2.55s	14357s	11673s

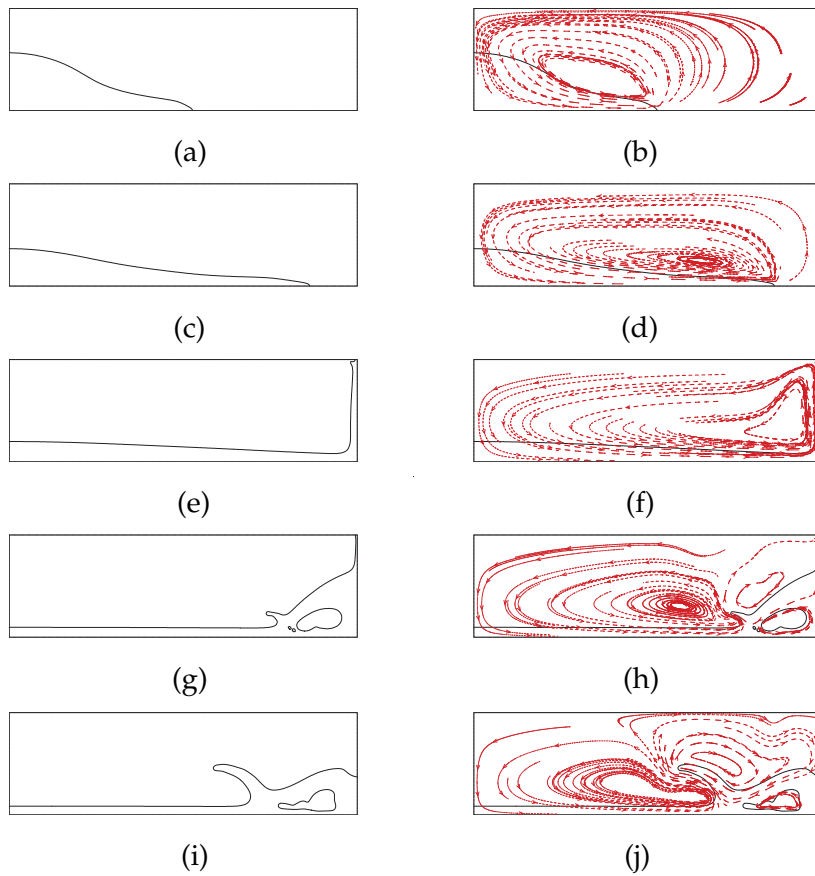Figure 10: The predicted free surfaces and streamfunctions for the dam break problem with 400×100 grids. (a), (b) $t = 1.5$; (c), (d) $t = 2.5$; (e), (f) $t = 4.0$; (g), (h) $t = 7.0$; (i), (j) $t = 7.8$.
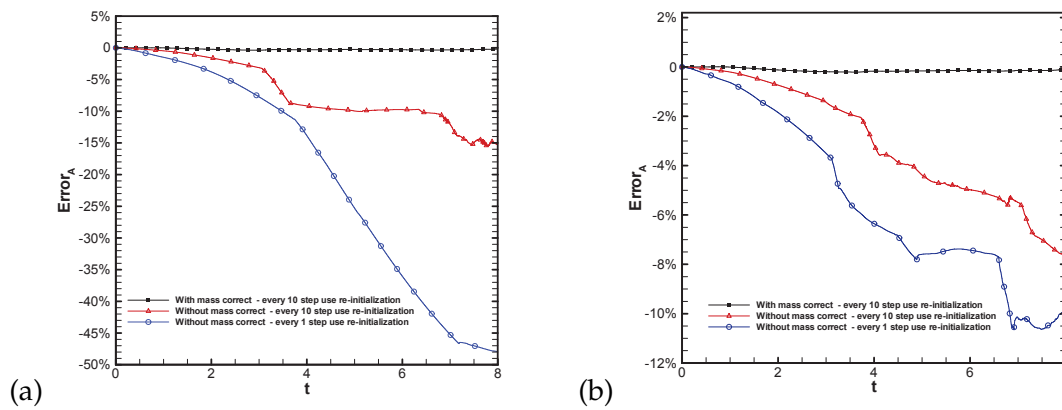

Figure 11: The computed area errors for the dam-break problem investigated in two grids. (a) 200×50 grids; (b) 300×75 grids.
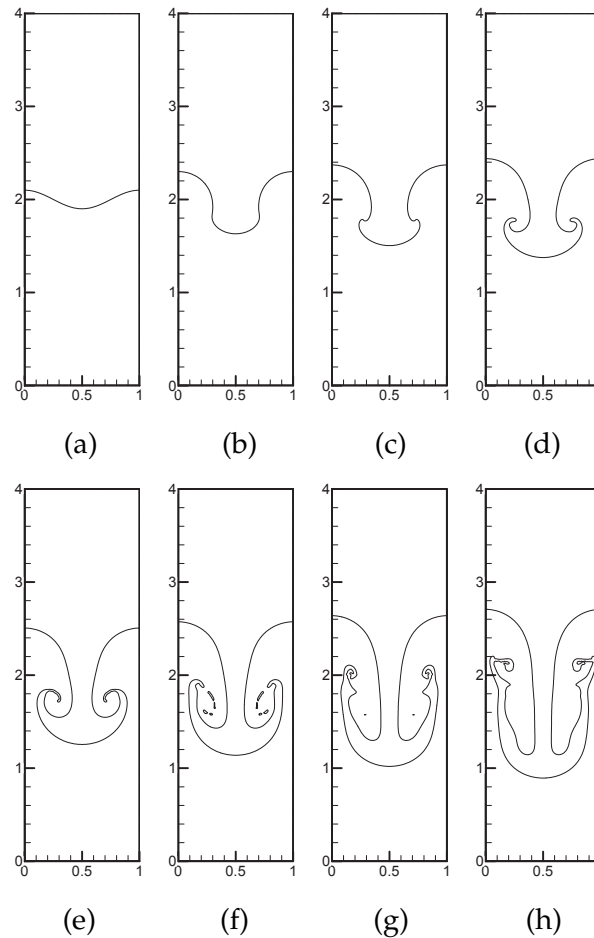
Figure 12: The predicted free surfaces at different times for the Rayleigh-Taylor problem investigated in 100×400 grids. (a) $t=0.0$; (b) $t=1.0$; (c) $t=1.25$; (d) $t=1.5$; (e) $t=1.75$; (f) $t=2.0$; (g) $t=2.25$; (h) $t=2.5$.

6.1.2 Rayleigh-Taylor problem

Rayleigh-Taylor instability may arise in conditions when a heavy fluid penetrates into a light fluid along the direction of gravity. Such a phenomenon has been observed in many scientific and environmental fields and has, therefore, been intensively studied [35]. The density difference is normally represented by the *Atwood ratio* $(\equiv(\rho_h-\rho_l)/(\rho_h+\rho_l))$. We validate our code here by investigating the same problem as did in Guermond et al. [36] at the values of *Atwood ratio* $=0.5$ and *Re* $(\equiv\rho_h l^{3/2}g^{1/2}/\mu)=3000$. Two incompressible fluids with the viscosities $\mu_h=1$ and $\mu_l=1$ are simulated in the rectangle of $0\leq x\leq1$, $0\leq y\leq4$. The initial condition is given by $y(x)=2+0.1\cos(2\pi x)$.

A no-slip condition is enforced at the bottom and top walls while the symmetry condition is imposed on the two vertical sides. The time evolving interfaces of the density field are plotted in Fig. 12, $t=0$, 1.0, 1.25, 1.5, 1.75, 2.0, 2.25 and 2.5. As before, the area
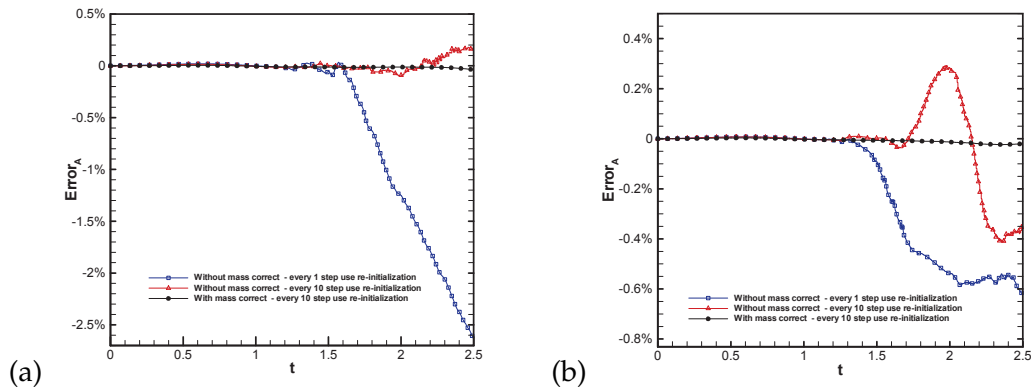
Figure 13: The computed area errors for the Rayleigh-Taylor problem investigated in two grids. (a) 50×200 grids; (b) 100×400 grids.

errors $Error_A$ predicted in conditions with/without re-initialization correction procedure are also plotted in Fig. 13. Good agreement with the numerical result given in [36] is clearly demonstrated in Fig. 14 for the predicted water height. As before, we compare the required CPU times using the current scheme, which invokes re-initialization only for every $10\Delta t$, and the conventional scheme, which needs re-initialization for each Δt, in Table 1.
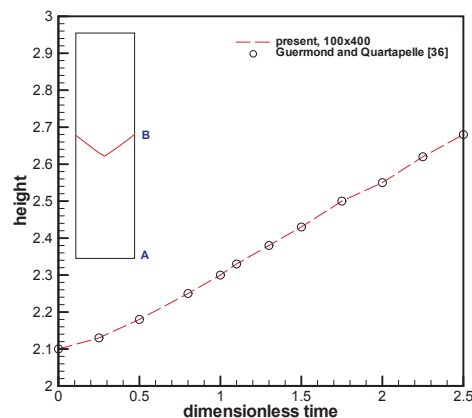

Figure 14: Comparison of the predicted heights (or the length $\overline{AB}$) of the lighter liquid on the right side of the water tank.

6.2 Interface prediction with surface tension

6.2.1 Two-dimensional double bubble rising in a partially filled container

The time-evolving interface problem, for which the surface tension needs to be taken into account, is then investigated. The problem under current investigation considers
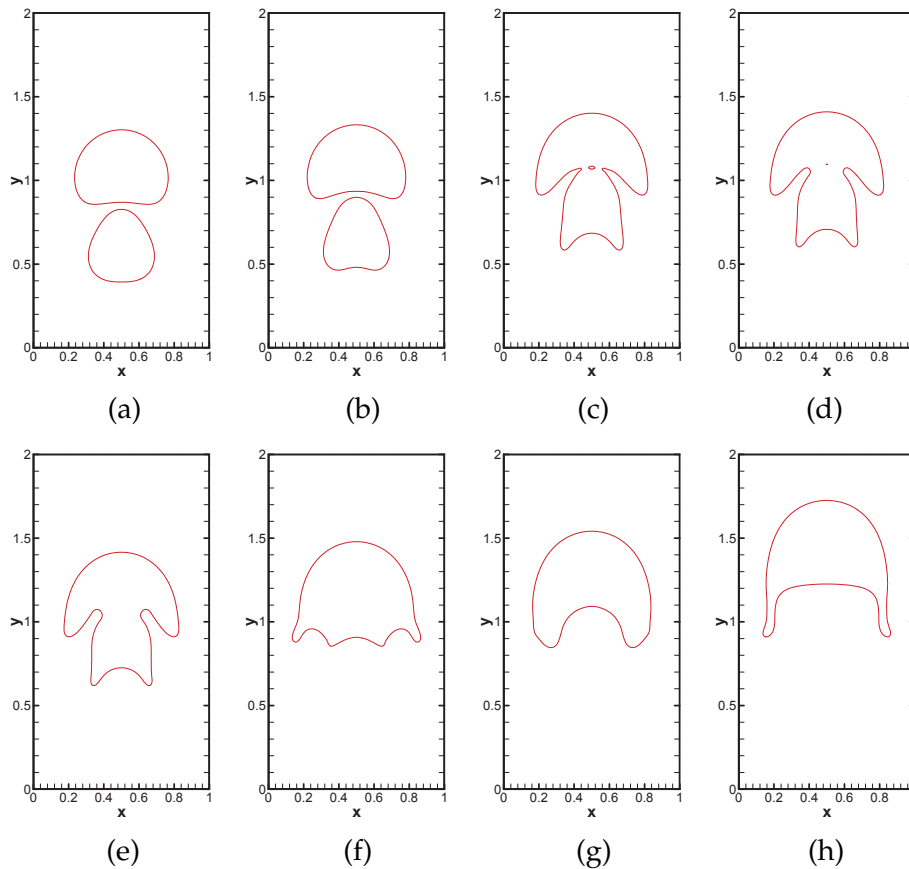
Figure 15: The predicted free surfaces at different times for the double bubble rising problem investigated in 140×280 grids. (a) $t=0.4$; (b) $t=0.6$; (c) $t=0.93$; (d) $t=0.97$; (e) $t=1.0$; (f) $t=1.3$; (g) $t=1.6$; (h) $t=2.5$.

the evolution of a stationary bubble, that is driven by surface tension, in a partially filled container. Here we consider the rectangular domain of $0 \le x \le 1$ and $0 \le y \le 2$, within which there are two circular bubbles. The centre of the first bubble is located at $(0.5,1.0)$ and its radius is equal to 0.25. The center of the second bubble is at $(0.5,0.5)$ and the radius is 0.2. We assume zero velocity field at the initial moment and the no-slip conditions are specified along the horizontal and vertical walls. The non-dimensional parameters chosen for this test are $Re=200$ and $We=100$. The fluid-gas density and viscosity ratios are specified respectively as $\rho_l/\rho_g=100$ and $\mu_l/\mu_g=10$.

In Fig. 15 the predicted free surface and bubble interface are plotted at 0.4, 0.6, 0.93, 0.97, 1.0, 1.3, 1.6 and 2.5. At $t=0.93$, two bubbles are merged into a single one. At this time, along the interface a cusp singularity is formed and it will be rapidly smeared by fluid viscosity and surface tension. Excellent area preservation can be seen clearly from Fig. 16. The save in the required CPU times can be seen clearly in Table 1 for this benchmark problem.
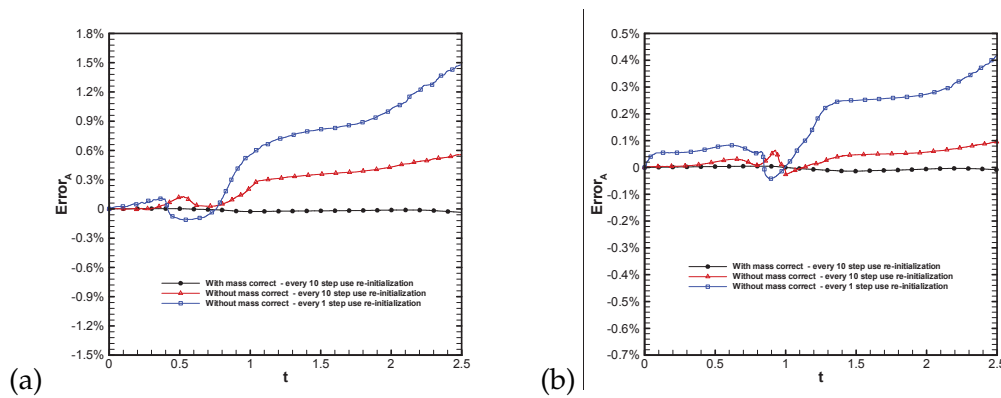
(a)   (b)

Figure 16: The computed area errors for the double bubble rising problem investigated in two grids. (a) 70×140 grids; (b) 140×280 grids.

6.2.2 Droplet falling in water

A water droplet falling through the air and hitting on the initially planar free surface will be investigated in this study. The dimensionless parameters chosen for this test are $Re = 7787$, $We = 55$ and $Fr = 1$. The fluid-gas density and viscosity ratios are specified
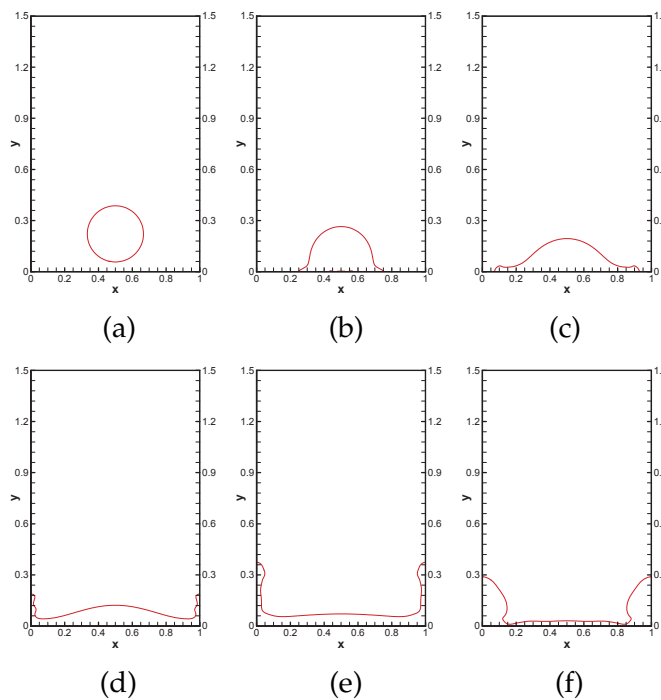

(a)   (b)   (c)

(d)   (e)   (f)

Figure 17: The predicted time-varying free surfaces for the droplet problem investigated in 140×210 grids. (a) $t = 1.25$; (b) $t = 1.35$; (c) $t = 1.425$; (d) $t = 1.55$; (e) $t = 1.75$; (f) $t = 2.55$.
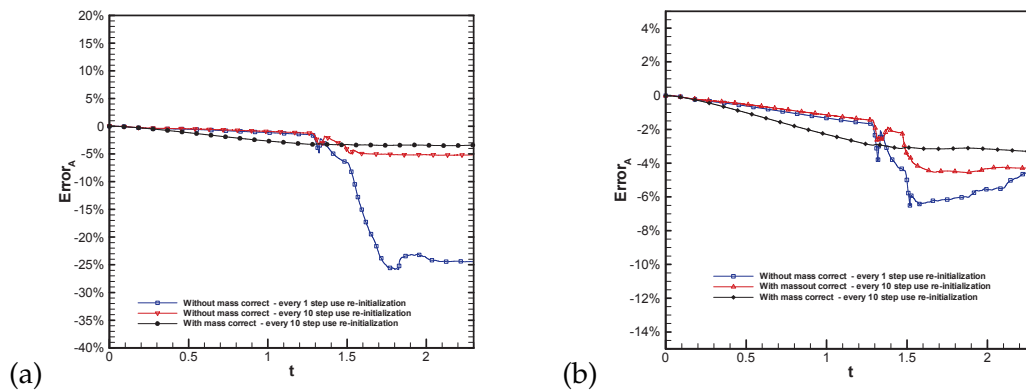
Figure 18: The computed area errors for the droplet problem investigated in two grids. (a) 100×150 grids; (b) 140×210 grids.

respectively at $\rho_l / \rho_g = 1000$ and $\mu_l / \mu_g = 100$. This droplet falling problem is performed in a box with the imposed no-slip solid wall boundary condition.

The droplet with its center located at $(0.5, 1.0)$ has a radius of $1/6$. In order to show the effect of grid refinement, calculations were carried out in the meshes with 100×150 and 140×210 nodal points. The predicted time-evolving droplet interface in the computational domain $0 \le x \le 1$ and $0 \le y \le 1.5$ is plotted in Fig. 17. As Fig. 18 shows, the area error $Error_A$ remains fairly small even in the case when the surface tension effect is taken into account. The comparison of the required CPU times, which involve every Δt in the conventional level set method and every ten Δt in the current scheme, is tabulated in Table 1.

7   Concluding remarks

Within the combined compact finite difference framework an upwinding advection scheme is developed for approximating the incompressible two-phase flow equations in non-staggered grids. The proposed level set method has been split into the equation, known as the conventional level set equation for the advection of level set function, and the re-initialization correction procedure. Since the area of the level set function is preserved, we employ the symplectic time-stepping scheme to approximate the time derivative term shown in the first-step of the level set equation so as to ensure the area-preservation property. The UCCD scheme with minimized phase error has been shown to be able to preserve interface shape excellently for the advection equation. In addition, our computational exercises show that the employed re-initialization process helps greatly to avoid mass loss or mass gain. The proposed spatial/temporal scheme with the respective accuracy orders of fifth and sixth has been used to solve three pure advection problems to demonstrate that both Hamiltonian conservation properties are indeed embedded in the discrete equation. Also, the chosen four benchmark problems with/without consid-

eration of surface tension have been numerically investigated with success to capture the interface in flow domains discretized by a moderate number of grid cells.

Acknowledgments

References

[1] J. A. Sethian and D. Adalsteinsson, An overview of level set methods for etching, deposition and lithography development, IEEE T. Semiconduct. M., 10(1) (1997), 167–184.
[2] C. R. Anderson, A vortex method for flows with slight density variations, J. Comput. Phys., 61(3) (1985), 417–444.
[3] J. M. Boultone-Stone and J. R. Blake, Gas bubbles bursting at a free surface, J. Fluid Mech., 254 (1993), 437–466.
[4] C. W. Hirt and B. D. Nichols, Volume of fluid method (VOF) for the dynamics of free boundaries, J. Comput. Phys., 39 (1981), 201–225.
[5] S. O. Unverdi and G. Tryggvason, A front-tracking method for viscous, incompressible, multi-fluid flows, J. Comput. Phys., 100 (1992), 25–37.
[6] V. E. Badalassi, H. D. Ceniceros and S. Banerjee, Computation of multiphase systems with phase field models, J. Comput. Phys., 190 (2003), 371–397.
[7] J. Kim, A continuous surface tension force formulation for diffuse-interface models, J. Comput. Phys., 204 (2005), 784–804.
[8] H. Ding, P. D. M. Spelt and C. Shu, Diffuse interface model for incompressible two-phase flows with large density ratios, J. Comput. Phys., 226 (2007), 2078–2095.
[9] J. A. Sethian and P. Smereka, Level set methods for fluid interfaces, Annu. Rev. Fluid Mech., 35 (2003), 341–372.
[10] C. W. Hirt, A. A. Amsden and J. L. Cook, An arbitrary Lagrangian-Eulerian computing method for all flow speeds, J. Comput. Phys., 135(2) (1997), 203–216.
[11] F. Harlow and J. Welch, Volume tracking methods for interfacial flow calculations, Phys. Fluids, 8 (1965), 21–82.
[12] S. Osher and J. A. Sethian, Fronts propagating with curvature dependent speed: algorithms based on Hamilton-Jacobi formulation, J. Comput. Phys., 79 (1988), 12–49.
[13] E. Marchandise, J. F. Remacle and N. Chevaugeon, A quadrature-free discontinuous Galerkin method for the level set equation, J. Comput. Phys., 212 (2006), 338–357.
[14] D. Enright, R. Fedkiw, J. Ferziger and I. Mitchell, A hybrid particle level set method for improved interface capturing, J. Comput. Phys., 183 (2002), 83–116.
[15] M. Sussman, E. Fatermi, P. Smereka and S. Osher, An improved level set method for incompressible two-fluid flows, Comput. Fluids, 127 (1988), 663–680.
[16] M. Sussman and E. Puckett, A coupled level set and volume-of-fluid method for computing 3D and axisymmetric incompressible two-phase flow, J. Comput. Phys., 162 (2000), 301–337.
[17] J. Strain, Tree methods for moving interfaces, J. Comput. Phys., 151 (1999), 616–648.
[18] S. Osher and R. Fedkiw, Level Set Methods and Dynamic Implicit Surfaces, Springer-Verlag, Berlin, 2003.

[19] J. A. Sethian, Level Set Methods and Fast Marching Methods, Cambridge University Press, Cambridge, 2003.

[20] E. Olsson and G. Kreiss, A conservative level set method for two phase flow, J. Comput. Phys., 210 (2005), 225–246.

[21] E. Olsson, G. Kreiss and S. Zahedi, A conservative level set method for two phase flow II, J. Comput. Phys., 225 (2007), 785–807.

[22] P. C. Chu and C. Fan, A three-point combined compact difference scheme, J. Comput. Phys., 140 (1998), 370–399.

[23] D. W. Zingg, Comparison of high-accuracy finite-difference methods for linear wave propagation, SIAM J. Sci. Comput., 22(2) (2000), 476–502.

[24] C. K. W. Tam and J. C. Webb, Dispersion-relation-preserving finite difference schemes for computational acoustics, J. Comput. Phys., 107 (1993), 262–281.

[25] G. Ashcroft and X. Zhang, Optimized prefactored compact schemes, J. Comput. Phys., 190 (2003), 459–477.

[26] T. W. H. Sheu and P. H. Chiu, A divergence-free-condition compensated method for incompressible Navier-Stokes equations, Comput. Methods Appl. Mech. Eng., 196 (2007), 4479–4494.

[27] R. I. McLachlan, Area preservation in computational fluid dynamics, Phys. Lett. A, 264 (1999), 36–44.

[28] M. Sussman, P. Smereka and S. Osher, A level set approach for computing solutions to incompressible two-phase flow, J. Comput. Phys., 114 (1994), 146–159.

[29] W. Oevel and W. Sofroniou, Symplectic Runge-Kutta schemes II: classification of symplectic methods, Univ. of Paderborn, Germany, Preprint, 1997.

[30] X. Zhong, High-order finite-difference schemes for numerical simulation of hypersonic boundary-layer transition, J. Comput. Phys., 144(2) (1998), 662–709.

[31] Y. Li, Wavenumber-extended high-order upwind-biased finite-difference schemes for convective scalar transport, J. Comput. Phys., 133 (1997), 235–255.

[32] Y. Wusi, C. L. Lin and V. C. Patel, Numerical simulation of unsteady multidimensional free surface motions by level set method, Int. J. Numer. Meth. Fluids, 42 (2003), 853–884.

[33] S. T. Zalesak, Fully multidimensional flux-corrected transport algorithms for fluids, J. Comput. Phys., 31 (1979), 335–362.

[34] J. C. Martin and W. J. Moyce, An experimental study of the collapse of liquid columns on a rigid horizontal plane, Philos. T. R. Soc. Lond., 224 (1952), 312–324.

[35] G. Tryggvason, Numerical simulations of the Rayleigh-Taylor instability, J. Comput. Phys., 75 (1988), 253–382.

[36] J. L. Guermond and L. Quartapelle, A projection FEM for variable density incompressible flows, J. Comput. Phys., 165 (2000), 167–188.